An Initial Assessment of a SMAP Soil Moisture Disaggregation Scheme Using TIR Surface Evaporation Data over the Continental United States

Vikalp Mishra[1*], W. Lee Ellenburg[1,2], Robert E. Griffin[3], John R. Mecikalski[3], James F. Cruise[1], Christopher R. Hain[4], Martha C. Anderson[5]

[1] Earth System Science Center, University of Alabama in Huntsville, Huntsville, Al-35805, USA; E-mail: vikalp.mishra@nsstc.uah.edu (VM); james.cruise@nsstc.uah.edu (JFC)

[2] NASA-SERVIR, National Space Science and Technology Center, Huntsville, Al-35805, USA; E-mail: lee.ellenburg@nasa.gov

[3] Atmospheric Science Department, University of Alabama in Huntsville, Huntsville, Al-35805, USA; E-mail: rgriffin@nsstc.uah.edu (REG); johnm@nsstc.uah.edu (JRM)

[4] NASA Marshall Space Flight Center, Earth Science Branch, Huntsville, AL, 35805, USA; E-mail: christopher.hain@nasa.gov

[5] Hydrology and Remote Sensing Laboratory, USDA Agricultural Research Services, Beltsville, MD, 20705, USA; E-mail: Martha.anderson@ars.usda.gov

Abstract

The Soil Moisture Active Passive (SMAP) mission is dedicated toward global soil moisture mapping. Typically, an L-band microwave radiometer has spatial resolution on the order of 36-40 km, which is too coarse for many specific hydro-meteorological and agricultural applications. With the failure of the SMAP active radar within three months of becoming operational, an intermediate (9-km) and finer (3-km) scale soil moisture product solely from the SMAP mission is no longer possible. Therefore, the focus of this study is a disaggregation of the 36-km resolution SMAP passive-only surface soil moisture (SSM) using the Soil Evaporative Efficiency (SEE) approach to spatial scales of 3-km and 9-km. The SEE was computed using thermal-infrared (TIR) estimation of surface evaporation over Continental U.S. (CONUS). The disaggregation results were compared with the 3 months of SMAP-Active (SMAP-A) and Active/Passive (AP) products, while comparisons with SMAP-Enhanced (SMAP-E), SMAP-Passive (SMAP-P), as well as with more than 180 Soil Climate Analysis Network (SCAN) stations across CONUS were performed for a 19 month period. At the 9-km spatial scale, the TIR-Downscaled data correlated strongly with the SMAP-E SSM both spatially (r = 0.90) and temporally (r = 0.87). In comparison with SCAN observations, overall correlations of 0.49 and 0.47; bias of -0.022 and -0.019 and unbiased RMSD of 0.105 and 0.100 were found for SMAP-E and TIR-Downscaled SSM across the Continental U.S., respectively. At 3-km scale, TIR-Downscaled and SMAP-A had a mean temporal correlation of only 0.27. In terms of gain statistics, the highest percentage of SCAN sites with positive gains (> 55%) was observed with the TIR-Downscaled SSM at 9-km. Overall, the TIR-based downscaled SSM showed strong correspondence with SMAP-E; compared to SCAN, and overall both SMAP-E and TIR-

Downscaled performed similarly, however, gain statistics shows that TIR-Downscaled SSM slightly outperformed SMAP-E.

Keywords - SMAP, Soil moisture, Disaggregation, ALEXI, MW-TIR coupling

1. Introduction

Soil moisture is an essential component of both the hydrologic and energy budgets. The amount of moisture in the soil drives a wide variety of hydrological, geotechnical, agricultural, and meteorological processes (Romano, 2014). Soil moisture (SM) can be estimated through ground based *in-situ* measurements, biophysical and land surface models (LSMs), or through remote sensing techniques. Existing ground based soil moisture networks are too sparse to provide accurate large-area assessments (Aghakouchak et al., 2015); therefore, LSMs offer the most common source for spatially distributed SM estimates. However, LSMs can be subject to error and bias and for this reason, other sources of SM data have been developed to aid in the correction of model inaccuracies. In particular, remote sensing technologies and land data assimilation techniques have come to the forefront to address these issues.

Microwave (MW) sensors, since their inception in late 1970s, have been used to estimate large scale surface SM (SSM), typically from higher frequency C-band [~6 GHz] and X-band [~10 GHz] sensors such as the Scanning Multichannel Microwave Radiometer (SMMR) (Owe et al., 2001); Special Sensor Microwave/Imager (SSM/I) (Paloscia et al., 2001); and the Advanced Microwave Scanning Radiometer (AMSR-E) (Njoku et al., 2003). Sensors such as the Soil Moisture and Ocean Salinity (SMOS) (Kerr et al., 2010) instrument and the Soil Moisture Active Passive (SMAP) (Entekhabi et al., 2010a) are the only missions dedicated toward global SSM

mapping operating at L-band [~1 GHz] frequencies. Low frequency L-band radiometers have penetration depths of approximately 3-5 cm and are sensitive to soil moisture through moderately thick vegetation water content (<5 kg/m^2) (Entekhabi et al., 2010a). Although exhibiting relatively higher accuracy and attenuated atmospheric absorption compared to the C- and X-bands, the L-band MW radiometer spatial resolution is on the order of 36-40 km (Merlin et al., 2015). Such spatial resolutions are acceptable for hydro-climatological studies but are known to be too coarse for many hydro-meteorological and agricultural applications (Brown et al., 2013).

The active sensors such as synthetic aperture radar (SARs) on the other hand can provide relatively higher spatial resolution than radiometers. Despite offering higher spatial resolution the active radars are typically limited by swath width and sensitive to even sparse vegetation cover thus tend to contain higher error/uncertainties than radiometers (Das et al., 2011). The SMAP mission, therefore aimed to combine both a high accuracy moderate resolution radiometer with a higher resolution but relatively less accurate radar on board a single platform to develop an integrated SSM product at intermediate resolution of 9-km with radiometer-like accuracy of 0.04 m^3/m^3 (Das et al., 2011; Entekhabi et al., 2010a).The integration of active and passive MW observations has been used as a disaggregation scheme to reduce the spatial footprint of coarse resolution radiometers with some success (Bindlish et al., 2009; Das et al., 2011; Narayan and Lakshmi, 2008; Rudiger et al., 2016). However, the SMAP radar malfunctioned within three months of it becoming operational and now been classified as legacy product with no further active efforts towards its retrieval. An alternate data stream distinct, from the original merged active-passive product, continues at intermediate spatial scale (9-km) called the SMAP-Enhanced (SMAP-E). The SMAP-E SSM is developed through an antenna gain

87 pattern analysis to achieve data interpolation from the original 11-km radiometer scale
88 instantaneous field-of-view (IFOV) paths (Chan et al., 2017).

89 Given the limitations of current passive MW SM missions to obtain fine-scale (<5-km)
90 SSM, several methods are under development, or have been developed, involving the use of finer
91 resolution active MW data from other instruments. In particular, the Sentinel-1 (A and B) data
92 stream has been identified by Das et al., (2016) as a primary candidate to replace the SMAP
93 radar. However, current efforts in this regard have either concentrated on enhancement of lower
94 resolution SMAP products (Santi et al., 2018) or have achieved only modest (and statistically
95 insignificant) improvements to the 9 km product (Lievens et al., 2017). Recently a beta version
96 of finer (1 and 3-km) resolution SM product (SPL2SMAP_S) (Colliander, 2017; Das and
97 Dunbar, 2017) has been developed using sentinel-1(A and B) and SMAP-E and added to the
98 suits of SMAP products. The availability of finer scale product is limited by Sentinel swath
99 width coverage.

100 Prior to the launch of the SMAP mission, several efforts were underway to downscale coarse
101 resolution MW SSM data to operational scales. One such approach was to employ visible and
102 thermal infrared (TIR) imagery to downscale (or disaggregate) the low resolution MW data.
103 Shorter wavelengths in the visible or infrared range can deduce SM through its relationship
104 between evapotranspiration (ET) and SM over a wide range of vegetation canopies (Anderson et
105 al., 2007). Several methods have been developed involving the use of finer resolution visible and
106 TIR imagery. Such approaches are based on the apparent triangle/trapezoidal pattern relationship
107 between land surface temperatures (LST) and vegetation indices (VI) linked with underlying
108 moisture content (Carlson, 2007; Carlson et al., 1981). Multiple variants of the triangle approach
109 have been studied and applied either directly as polynomial fitting (Chauhan et al., 2003;

Knipper et al., 2017; Piles et al., 2016, 2011; Sanchez-Ruiz et al., 2014) or indirectly as evaporative fraction (Kim and Hogue, 2012; Merlin et al., 2012, 2008).

A variant of the triangle approach that is relatively more theoretically and physically-based than polynomial fitting was proposed by Merlin et al., (2010,2013, 2012) which relates the soil evaporative efficiency (SEE) to surface moisture content. SEE can be defined as a ratio of actual to potential soil evaporation (Fang and Lakshmi, 2014; Merlin et al., 2010). These authors used finer resolution MODIS VI, LST and surface albedo to compute SEE based on the triangle approach to generate a downscaled SMOS SSM product up to 1-km resolution in southern Australia (Merlin et al., 2012). Multiple recent studies have used the SEE-based algorithm to downscale SSM from AMSR-E, SMOS and SMAP with some success, albite over limited spatial domains: Chan et al., (2017); Colliander et al., (2017); Djamai et al., (2015); Malbéteau et al., (2016); Molero et al., (2016), and Mishra et al., (2017). A comparative study of multiple disaggregation schemes by Kim and Hogue, (2012) in the semi-arid climatic conditions of the Western United States indicated that the SEE-based disaggregation technique performed better than the empirical polynomial fitting approach. One of the limitations of the visible (VIS)/infrared (IR) based disaggregation is the lower cloud penetration capabilities of such bands, resulting in data gaps under cloudy conditions. Multiple other downscaling algorithms exist and an excellent review of SSM downscaling approaches is presented by Peng et al., (2017).

In this study, the SEE-based algorithm from Merlin et al., (2012) was used to disaggregate the SMAP radiometer SSM product over CONUS and compared to the available higher resolution SMAP SSM products and to in situ data. The purposes of the study are twofold: first to evaluate the higher resolution (3- and 9-km) SMAP SSM against a popular TIR-based

downscaling scheme thus comparing the SMAP interpolations against a more physical method; and second to evaluate finer resolution products from SMAP and TIR-based against in situ observations across the CONUS encompassing a variety of ecosystem and climate conditions. In this study the SEE was computed directly from surface actual evaporation and potential surface evaporation data. The TIR-based Atmospheric Land Exchange Inverse (ALEXI) model (Anderson et al., 1997, 2011) was used to obtain actual surface soil evaporation. Potential surface evaporation, defined here as the atmospheric demand, is computed using Hamon PET (Hamon, 1963) and is independent of the underlying soil and plant characteristics and therefore, acts as a proxy for potential surface evaporation.

The disaggregation of the SMAP radiometer SSM estimates was performed over CONUS from Apr. 2015 – Nov. 2016 at 9 and 3-km spatial resolutions. The specific objectives of this study are: (a) to apply the TIR-driven disaggregation algorithm to downscale coarse scale SMAP radiometer SSM to finer scale (9 and 3-km) SSM; (b) to evaluate the SEE disaggregation method over a large spatial domain encompassing multiple ecosystems; (c) to evaluate the TIR driven disaggregation scheme against the SMAP SSM products at corresponding spatial scales (9 km and 3 km); and (d) to evaluate and intercompare the SMAP products and TIR-Downscaled SSM against *in situ* SSM observations across the CONUS. Evaluation of the 3-km product can serve to inform current efforts in combining active and passive radars to achieve finer resolution SM products.

3. Data Description

3.1 SMAP Soil Moisture Data

155 The coarse resolution L-band MW SSM product from SMAP-Passive (SMAP-P) was used as
156 an input to the disaggregation algorithm. Whereas the intermediate [9-km SMAP-Active/Passive
157 (AP) and SMAP-Enhanced (E)] and fine [3-km SMAP-Active (A)] SSM products from the
158 SMAP mission were used for comparison and evaluation purposes. The Active radar (SMAP-A)
159 and SMAP-AP products are available from April 2015 to July 2015 (88 days), while the SMAP-
160 P and SMAP-E SSM products are available from March 2015 to present. The Level-3 daily
161 SMAP products are projected over fixed ease-grid at 36-km (Passive), 9-km (Active/Passive &
162 Enhanced) and 3-km (Active) resolutions. The 1,000-km wide swath allows SMAP 2-3 day
163 global revisit.

164 **3.2 ALEXI Surface Evaporation**

165 The ALEXI model is an energy balance model that utilizes time differential rise in morning
166 LST data from Geostationary Operational Environmental Satellites (GOES) to retrieve actual
167 evapotranspiration (ET) (Anderson et al., 2007; Hain et al., 2012). The land-surface
168 representation in ALEXI model is a two-source model that estimates the partitioning of surface
169 evaporation and plant transpiration from the total system ET. Although the model is processed at
170 a daily time step, direct retrievals of ALEXI surface evaporation are available only on
171 substantially cloud-free locations within a GOES satellite's field-of-view (Hain et al., 2011;
172 Mishra et al., 2013).

173 A continental scale implementation of the TIR-based ALEXI model was used in this study.
174 The ALEXI model operates at 0.04^0 (4.7-km approx.) spatial resolution over CONUS. The 4.7-
175 km ALEXI product is ideal for this study since its resolution falls neatly between the 3-km and
176 9-km SMAP products. The gridded surface evaporation from ALEXI was resampled to 3 and 9-

177 km consistent with the SMAP resolution using the nearest neighbor technique. The ALEXI
178 model errors typically ranges from 15-20% at the 4-km scale and 5-10% on the field-scale
179 compared to flux tower observations (Anderson et al., 2011).

180 **3.3 NRCS SCAN Observations**

181 Ground-based observations of surface volumetric SM were available from Natural Resources
182 Conservation Services Soil Climate Analysis Network (SCAN) sites. A total of 228 active SCAN
183 sites are present in the study area; however, not all stations reported surface SM data over the
184 study period. SCAN stations periodically monitor multiple meteorological parameters such as
185 precipitation, air temperature, relative humidity, *etc.* along with SM and temperature at various
186 depths at near real time with hourly and/or daily sampled time steps. This study utilizes the SM
187 measurement from the top 2 inches (~5 cm) acquired using a Hydra Probe instrument (Schaefer
188 et al., 2007). The SCAN sites, despite having low density compared to the gridded 3 to 36 km
189 footprints of satellite-derived SM datasets, cover a wide range of soil and climatic conditions
190 across the CONUS. Figure 1 shows the location of all the active sites used in this study within
191 the CONUS.

192 **3.4 Ancillary Datasets**

193 In addition to above mentioned data, gridded daily air temperature and SSM data from a
194 LSM were also used in this study. The North America Land Data Assimilation System
195 [NLDAS2; (Xia et al., 2012)] air temperature forcing data at 0.125^{o} resolution was used to
196 compute Hamon PET, while the SSM product was also used in this study to further evaluate the
197 performance of remotely sensed SSM products. Terrain adjustment of coarse resolution
198 temperature data was performed using a 30-m digital elevation map [GTOPO30 digital elevation

model, (Miliaresis and Argialas, 1999)] with a constant lapse rate for the study region. The GTOPO30 elevation map for the CONUS was obtained from the U.S. Geological Survey's EROS Data Center. The coarse resolution SSM data from NLDAS2 were resampled using nearest neighbor scheme to match the respective remotely sensed SSM resolution. Table-1 summarizes the various datasets used in this study.

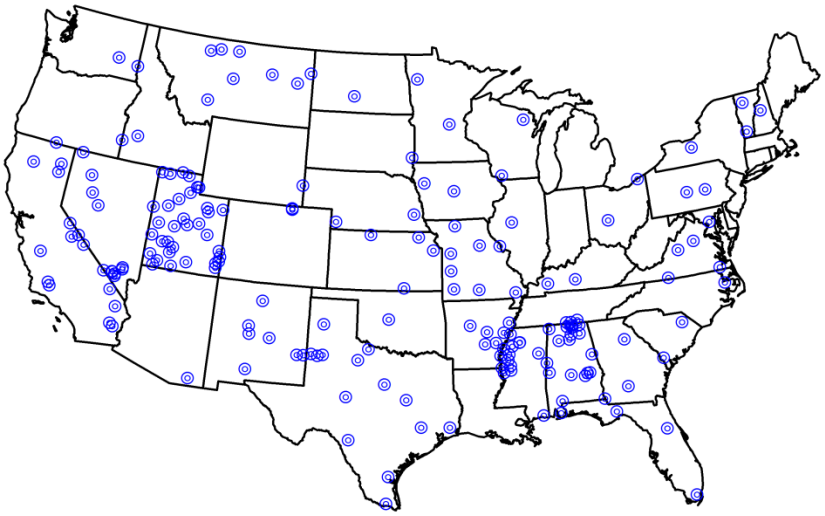

Figure 1: Continental United States with active NRCS SCAN site locations

Table 1: A summary of data sources used in the study with their description and temporal ranges used.

Data Source	Description	Spatial Resolution	Temporal Resolution	Data period	No. of days
SMAP - A	Active Radar only SM	3-km	2-3 days	Apr 2015 – Jul 2015	88
SMAP-P	Passive Radiometer only SM	36-km	2-3 days	Apr 2015 – Nov 2016	607
SMAP-AP	Merged active-passive SM	9-km	2-3 days	Apr 2015 – Jul 2015	84
SMAP-E	Enhanced SM product	9-km	2-3 days	Apr 2015 – Nov 2016	607
SCAN	*In-situ* SM observations	Point data (182 stations)	Hourly and daily means	Apr 2015 – Nov 2016	607
ALEXI	TIR-based model surface Evaporation	4.7–km	Daily	Apr 2015 – Nov 2016	607

4. Methodology

4.1 Surface SM Disaggregation

With the early mission malfunctioning of the SMAP radar, the search for effective alternatives is of high priority within the agricultural and hydro-meteorological communities (Chen et al., 2017). A semi-empirical, physically based disaggregation scheme introduced by Merlin et al. (2012, 2013, 2008), called DISaggregation based on Physical And Theoretical scale CHange (DISPATCH), was used in this study. The disaggregation approach is depended on underlying SEE, which is a model used to map surface evaporative fluxes to the moisture content at finer scales. Its basic premise is that the SEE is scale invariant and related to surface SM. As pertinent to this study we re-present the equation of the scheme that reflects the fundamental theoretical basis of the algorithm:

$$SSM_{HR} = SM_{LR} + M_{LR}[SEE_{LR} - \langle SEE_{HR} \rangle_{LR}] \quad (1)$$

Here, HR and LR refer to high and low resolution variables, respectively. The SEE is computed initially at the native ALEXI higher resolution (0.04^{o}) and then resampled to lower resolutions. M is the partial derivative function that relates SEE to the underlying SM content. $\langle SEE_{HR} \rangle_{LR}$ is high resolution SEE aggregated to low resolution MW scale.

Multiple models have been proposed in the past that describe the relationship between SEE and surface moisture content. In earlier studies, Merlin et al., (2012, 2008) employed variants of non-linear relationships by Lee and Pielke (1992); Noilhan and Planton (1989); Komatsu (2003). A comparative study by Merlin et al. (2010b) suggests that the non-linear model by Noilhan and Planton (1989) was superior to the other non-linear models. Recent studies by authors such as Merlin et al. (2013, 2015) and Djamai et al. (2015) showed that a linear model performed better

than earlier proposed non-linear methods over relatively dry climatic conditions of South Australia and Spain. In this study, we originally applied both linear and non-linear models for disaggregation. However, the continental scale of the study area and contrasting climatic conditions resulted in very similar overall statistics over CONUS. In the majority of instances the f-test with 95% confidence interval showed no statistical difference between the statistics of the two models averaged over CONUS. Therefore for simplicity only the non-linear model is discussed in this study. The non-linear model suggested by Noilhan and Planton, (1989) is given as:

$$M_{LR} = \frac{SSM_{LR}}{cos^{-1}(1 - 2SEE_{LR})\sqrt{SEE_{LR}(1 - SEE_{LR})}} \quad (2)$$

4.1.1 Modified SEE computation

SEE can be defined as a normalized surface evaporation. In the original DisPATCH model, the SEE is computed based on the triangle approach using MODIS LST, VI and surface albedo. However in this study, the SEE was computed directly from the ALEXI actual surface evaporation and computed potential surface evaporation:

$$SEE = \frac{E_s}{PE_s} \quad (3)$$

Here, E_s *and* PE_s refers to actual surface evaporation and potential surface evaporation, respectively. The *SEE* is computed at spatial resolution corresponding to the resolution of actual evaporation data. The surface actual evaporation was obtained from the ALEXI model and the potential ET (PET) was estimated using the Hamon PET model (Hamon, 1963) as a proxy for PE_s. Hamon PET is solely dependent upon atmospheric demands that are completely decoupled

from the underlying soil and canopy characteristics. Therefore, the model can be used as a proxy of PE_s. The Hamon PET is computed as:

$$H_{PET} = K.(35.755).N.\frac{e_s}{T + 273.3} \quad (3)$$

K is the proportionality constant used as 1, N is the daylight hours in multiples of 12 and e_s is the saturated vapor pressure at the given temperature T $(°C)$ which is given as: $6.108\, e^{\frac{17.26\,T}{(237.3+T)}}$, where T is the mean daily temperature. The terrain-adjusted daily min/max temperatures from the NLDAS2 forcing data are used to compute daily mean temperatures. Terrain adjustment of the coarse resolution temperature data were performed using a 30 m digital elevation map of the region and a constant lapse rate of -6.5 K km^{-1} (Cosgrove, 2003).

4.2 Evaluation Matrices

The 2-3 day revisit cycles of the SMAP and cloud constraints on ALEXI make both datasets prone to data gaps at a daily time-step. Recent studies such as (Leng et al., 2017a, 2017b) explored a gap filling algorithm based on canopy surface and aerodynamic coefficients obtained using satellite and meteorological data. Although this approach has shown promise, it requires ancillary data sets that were not otherwise used in this study (e.g. wind speed) and that could introduce further sources of error into the analyses. On the other hand, although SM content at the surface is the most variable across depth temporally (Brocca et al., 2010; Starks et al., 2003), recent studies by Penna et al., (2013) showed that the SM dynamics at shallow depths (~0-10 cm) are strongly correlated for temporal lags less than 5 days. Further, satellite data can be noisy at a daily time step; thus, temporal compositing can be used to reduce daily variability while retaining the temporal dynamics of the SSM (Anderson et al., 2011). Therefore, a 3-day

centered moving window compositing was performed to fill in some of the data gaps associated with remotely sensed SSM datasets.

The data gaps in all three datasets restrict time series analysis, hence pair-wise spatial and temporal statistical comparisons were performed using traditional matrices such as: bias, root mean squared difference (RMSD) and correlation coefficient (r). It has been argued that the traditional RMSD can be overestimated if a bias exists either in model or reference dataset (Entekhabi et al., 2010b). Therefore, an unbiased estimation of RMSD (ubRMSD) is computed by removing the potential impact of bias in the error estimation. The ubRMSD can be computed as:

$$ubRMSD = \sqrt{E\{[(\theta_{est} - E[\theta_{est}]) - (\theta_{ref} - E[\theta_{ref}])]^2\}} \quad (5)$$

where, E[:] is the expectation operator, θ_{est} and θ_{ref} are SM values estimated and reference (or observed), respectively.

As there is a spatial mismatch involved in comparing gridded SSM estimations with *in-situ* observations, sampling errors can occur (Peng et al., 2017). Multiple upscaling algorithms have been suggested for sparse *in-situ* monitoring stations to minimize the impact of sampling error; however, these methods typically require a dense network of such stations in addition to an independent *a-priori* error characterization (Crow et al., 2012). One possible alternative is the computation of gain statistics. Merlin et al., (2015) have proposed a performance matrix to compute relative gain in slope, correlation and biases to measure the overall improvement of downscaled SSM estimates over coarse resolution data with reference to a given set of point observations. The gain is the measure of improvement (or degradation) in the statistics obtained with fine scale and *in-situ* pair with respect to coarser scale and *in-situ* pair. The value of gain

can range from -1 to 1; with gain > 0 indicating a better correspondence of disaggregated SSM data than coarser scale with respect to *in-situ* observations and *vice-versa.* The gain in slope represents the improvement (or degradation) in efficiency of the disaggregated SSM to represent *in-situ* observations compared to original coarser scale SSM data. Similarly, the gain in bias and correlation represent the improvement (or degradation) of accuracy and precision, respectively. The relative gain in slope (G_{Eff}: efficiency gain); gain in correlation coefficient (G_{Prec}: precision gain); and gain in bias (G_{Acc}: accuracy gain) are computed as:

$$G_{Eff} = \frac{|1 - S_{LR}| - |1 - S_{HR}|}{|1 - S_{LR}| + |1 - S_{HR}|} \quad (4)$$

$$G_{Prec} = \frac{|1 - R_{LR}| - |1 - R_{HR}|}{|1 - R_{LR}| + |1 - R_{HR}|} \quad (5)$$

$$G_{Acc} = \frac{|B_{LR}| - |B_{HR}|}{|B_{LR}| + |B_{HR}|} \quad (6)$$

Here *LR* refers to low resolution SSM statistics [S: slope; R: Correlation and B: Bias] against *in-situ* observations whereas *HR* refers to the statistics of the high-resolution SSM against the *in-situ* observations. The gains in slope, bias and correlations are partial gains, whereas overall gain (G_{Down}) can be represented as a simple unweighted mean of the partial independent relative gains (Merlin et al., 2015). Relative gain statistics are advantageous over traditional statistics in that they measure the relative performance of two SSM datasets directly against the target data making it less sensitive to bias in the mean or in the variance. Relative gain also tends to reduce the uncertainties associated with the mismatch in spatial scales of *in-situ* and remotely sensed data (Merlin et al., 2015).

5. Results

317 The TIR-downscaled SSM data were compared and validated against remotely sensed SMAP
318 SSM products at corresponding resolutions along with in situ observations from SCAN sites
319 across CONUS. The disaggregation scheme described in section 4.1 and 4.2 was applied to the
320 coarse resolution SMAP radiometer SSM product over the CONUS and the disaggregated SSM
321 estimates were compared spatially and temporally against the available and corresponding
322 SMAP SSM products as well as SCAN site observations. The following section details the
323 results of comparisons and validation, first among remotely sensed products and then with in situ
324 observations. Figure 2 displays the composited SSM conditions from SMAP (P, A, AP, and E),
325 as well as the TIR-downscaled (3- and 9-km scales) for a single day (Julian day 159) during the
326 summer of 2015 over CONUS.
327

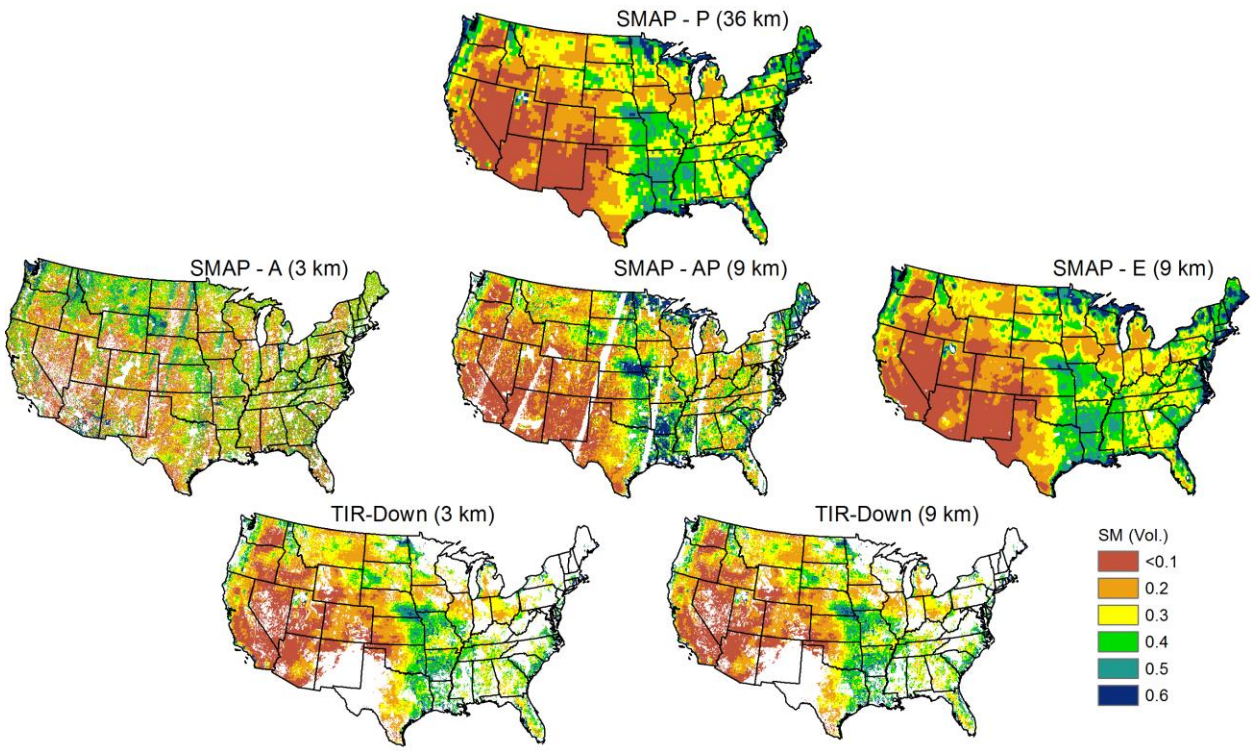

328
329 Figure 2: SSM estimates from SMAP at coarse resolution Passive (36-km); Active (3-km); Active/Passive (9-km);
330 and Enhanced product (9-km) compared with TIR-Downscaled SM data (3 and 9-km) on 8 June, 2015 for
331 demonstration purpose. The white spaces indicate no data availability.
332

5.1 Spatial Analysis

SSM products from SMAP (A, AP & E) and TIR-downscaled data (9- and 3-km resolutions) were compared over the CONUS grids and the average statistics over the study period are shown in Figure 3. At 9-km resolution, the mean spatial correlation (r) between SMAP-AP and TIR-downscaled SM was 0.76 with an overall ubRMSD of 0.09 m^3m^{-3} and a negative bias of -0.013 m^3m^{-3}. Compared with the SMAP-E SSM product, the TIR-Downscaled SSM showed average *r* of 0.90 with ubRMSD of 0.057 m^3m^{-3} and bias of -0.01 m^3m^{-3}. The SMAP-AP and SMAP-E SSM had *r* of 0.84, ubRMSD of 0.09 m^3m^{-3} and bias -0.003 m^3m^{-3}. The figure shows that the statistics between the SMAP-E and TIR 9-km products were relatively stable over the 19 month study period.

A similar grid analysis of the SSM signals was performed between SMAP-A (3-km) and TIR-downscaled (3-km) SSM estimates and the results are also shown in Figure 3. The similarity of the 3-km SSM products (SMAP-A vs TIR-Downscaled) was considerably weaker relative to the 9-km products. The average *r* between the SMAP-A (active radar) SSM measurement and TIR-based 3-km downscaled SSM was 0.29. The ubRMSD was found to be 0.14 m^3m^{-3} and bias was 0.008 m^3m^{-3}. The overall mean bias was close to zero (= 0.008 m^3m^{-3}) however the daily standard deviation (SD = 0.017 m^3m^{-3}) was double of the mean. It is noted that the statistics of the SMAP products where the active radar was employed are based on much smaller sample sizes (84-88 days) compared to the products without the active sensor and therefore it is difficult to make any concrete conclusions relative to these results.

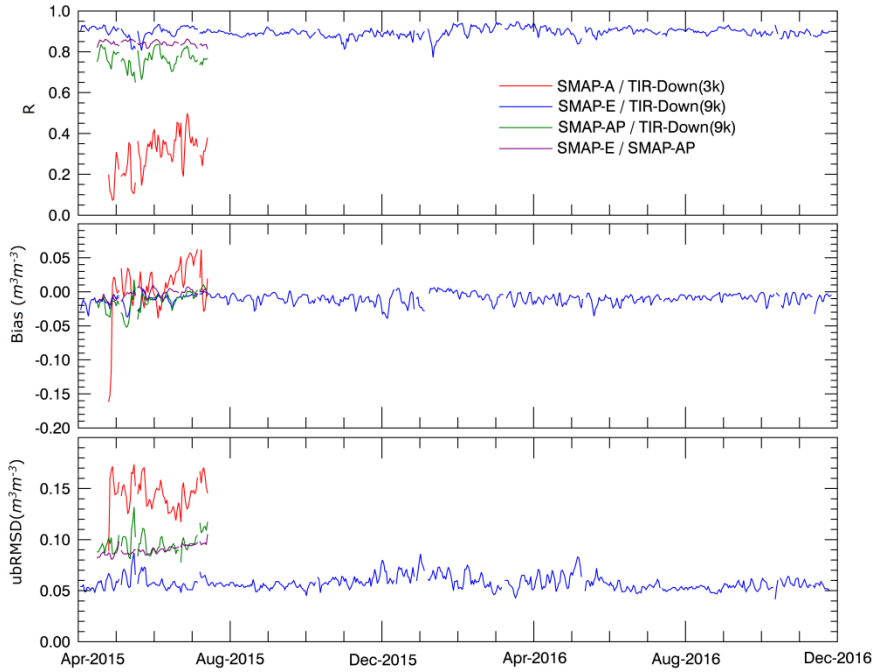

Figure 3: A daily time series of spatial correlation (top); bias (middle) and coefficient of ubRMSD (bottom) at 9-km and 3-km spatial scales over CONUS between SMAP and TIR-Downscaled SSM products.

5.2 Temporal Analysis

Temporal analysis at each pixel is limited by the number of days the corresponding SSM products coincide. Figure 4 shows the map of statistics at 9-km resolution between SMAP-AP, E and TIR-Downscaled SSM products over CONUS. The overall mean temporal correlation between SMAP-E and TIR-downscaled SSM over CONUS (right panel) was found to be 0.87 with ubRMSD of 0.03 m^3m^{-3} and bias at -0.03 m^3m^{-3}. Comparison with SMAP-AP the TIR-Downscaled SSM (middle panel) showed an overall *r* of 0.71, ubRMSD = 0.05 m^3m^{-3} and bias of 0.065 m^3m^{-3} temporally but for a sample size of only 84 days. The SMAP-AP compared with SMAP-E (left panel) showed *r* of 0.75 and ubRMSD of 0.04 m^3m^{-3} with bias = 0.06 m^3m^{-3} again with the smaller sample size.

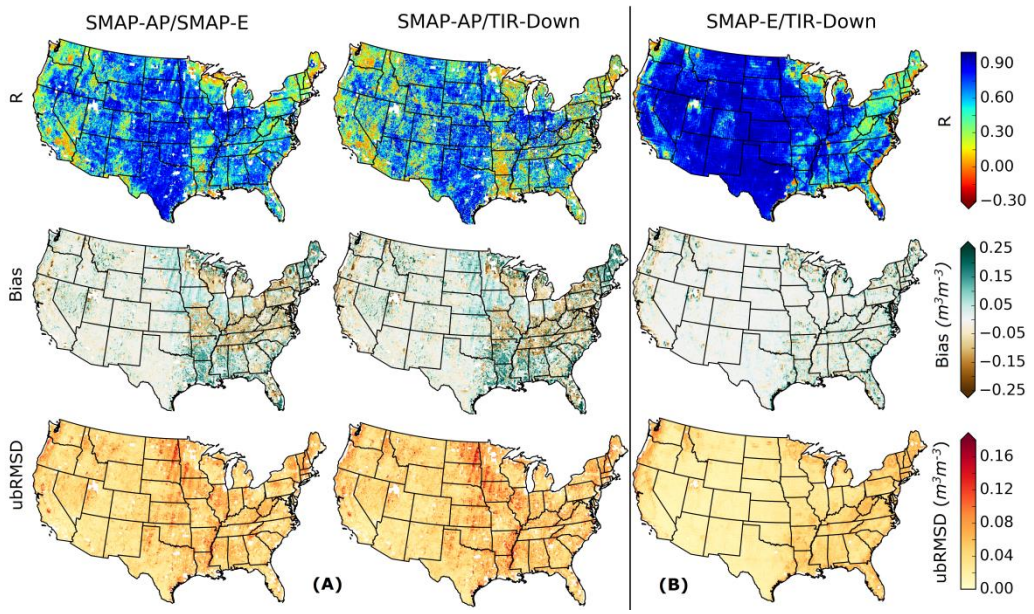

Figure 4: Map of CONUS displaying statistics between SMAP-AP, E and TIR-downscaled SM at 9-km scale: correlation coefficient (top); Bias (middle) and ubRMSD (bottom) distribution across CONUS for the period of Apr-June 2015 (left two panels); Apr 2015 - Nov-2016 (right panel)

These results indicate that the 9-km TIR-downscaled SSM most strongly relates to the SMAP-E with high correlation and low ubRMSD values followed by the SMAP-AP SSM product. Geographically, the figure demonstrates that the SMAP products correlate better among themselves as well as with the TIR SSM in the mid-west and western portions of CONUS than in the east and southeast with the exception of the pacific northwest where correlations were also low. This is particularly striking in the SMAP-E vs TIR analysis. In particular it is clear that the comparisons were poor in a band running from Maine along the Appalachian mountain chain into east Tennessee. This area is moderately-to-heavily forested often exhibiting steep slopes and thin soils overlaying limestone bedrock. It is an area where neither the radar nor ALEXI would be expected to perform well.

In terms of 3-km SSM products (SMAP-A vs TIR-Downscaled), r = 0.27, with an ubRMSD of 0.097 m^3m^{-3} and bias 0.011 m^3m^{-3}. Figure 5 shows the map of temporal statistics between the two SSM products. Though it can be seen from Figure 5 that both the 3-km SSM products are still most similar in the West-Central United States (with $r > 0.6$ and ubRMSD < 0.07 m^3m^{-3}), yet the distinction is not as clear as in the 9-km products of similar time frame. The overall bias at the 3-km scale is lower than the 9-km products [0.011 vs 0.065 (with SMAP-AP) and 0.028 (with SMAP-E) m^3m^{-3}], however the variance in bias across CONUS is 0.015 m^3m^{-3} which is 2 and 7 times higher compared to bias in SMAP-AP and SMAP-E, respectively. The higher variance in 3-km indicates a relatively greater spread and instability in results across CONUS despite the low overall mean bias. Again, it should be noted that these results are for a sample size of only 84 days while the 9-km results are based on a 19-month (607 days) sample size.

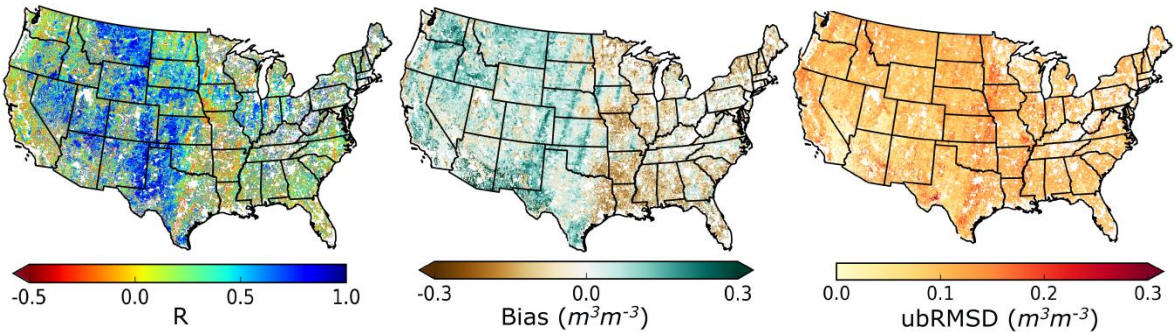

Figure 5: Statistics between SMAP-A and TIR-Downscaled SM at 3-km scale over CONUS.

5.3 Comparison with SCAN Observations

The remotely sensed SSM estimates from SMAP (A, AP, E & P) along with TIR-Downscaled (3 & 9-km) were compared with SCAN site in situ observations across CONUS. While comparing remotely sensed SSM to in situ observations, disparity of spatial scale as well as the sensing depths must be considered. Some authors prefer to remove the bias due to scale

difference before comparisons (Brocca et al., 2011); however, it is common practice to compare in situ observations without adjusting for scale even when only one observation per pixel is available (McCabe et al., 2005; Sahoo et al., 2008). In this study, remotely sensed SSM estimates are compared directly without bias correction or upscaling of in situ observations. Although, the absolute value of SSM varies spatially at much finer scales (~ few meters), the temporal dynamics are found to be highly correlated spatially, indicating that the temporal SSM dynamics can be compared between datasets of varied spatial scales (Seneviratne et al., 2010). In addition, the use of gain statistics can mitigate some of the scale disparity error (Merlin et al., 2015).

A total of more than 180 SCAN sites over CONUS were active and provided daily summaries of SM and other meteorological observations (such as, soil temperature, humidity, *etc.*) during the study period. SSM observations (≤ 2 inch (~5cm) depth) were collected from SCAN sites for comparisons with remotely sensed SSM products. Table 2 shows the overall statistics of the remotely sensed SSM compared with the SCAN observations over CONUS. The overall correlation between SCAN observations and coarse resolution SMAP-P SSM data was 0.54. Mean bias at all sites was -0.02 m^3m^{-3} and ubRMSD of 0.06 m^3m^{-3}. The intermediate resolution SMAP-E was found to have similar statistics although the correlation was slightly lower (r = 0.49). The finer resolution SSM data from the active radar on the other hand, showed relatively less similarity with SCAN observations (r = 0.16, ubRMSD = 0.077 m^3m^{-3}), although there is a slight improvement in overall bias compared to the coarser resolution SMAP-P and E estimates (0.008 vs -0.022 m^3m^{-3}). The SMAP-AP, a combination of passive and active, showed better agreement than SMAP-A but poorer agreement than SMAP-P. There is a slight disparity in sample size in case of SMAP-A & AP that should be taken into account while interpreting the results. The summary statistics with coincident data records are shown in appendix table A1.

Table 2: Summary statistics between remotely sensed SSM and SCAN observations across CONUS

SM Product	No. of sites	No. of Days	r	Bias (m^3m^{-3})	ubRMSD (m^3m^{-3})	Slope
SMAP – P	181	563	0.54	-0.021	0.062	0.47
SMAP – A	156	54	0.16	0.008	0.077	0.19
SMAP – AP	144	69	0.37	-0.006	0.069	0.49
SMAP – E	182	570	0.49	-0.022	0.062	0.40
TIR-Down (3k)	181	306	0.47	-0.019	0.064	0.42
TIR-Down (9k)	180	300	0.47	-0.019	0.064	0.41

The TIR-Downscaled SSM, when compared with SCAN observations, showed statistics similar to SMAP-P and -E products. It can be noticed that the statistics are identical for both the 3-km and 9-km resolutions. The overall ubRMSD increased slightly from 0.062 to 0.064 (m^3m^{-3}) but there is an improvement in bias (-0.022 to -0.019 m^3m^{-3}) compared to the SMAP-P SSM estimate. In addition, there was a slight decline in r for the downscaled SSM to 0.47 compared to 0.49 for the SMAP-E, but better than the 0.37 exhibited by the SMAP-AP (albeit with a much smaller sample size). Interestingly, the correlations of both the SMAP and TIR relatively finer scale products were less than that of the coarser SMAP-P product itself.

The overall results indicate that the downscaled SSM products, either SMAP-E or TIR-Downscaled, showed overall statistics similar to the coarse SMAP-P. In case of SMAP, the brightness temperature from the same source is being used with a similar algorithm to deduce passive and enhanced SSM products. The SMAP-E is merely an interpolation of the SMAP-P data. Therefore, similarities between the products are expected. The TIR-down, on the other hand uses TIR derived evaporative efficiency in addition to passive MW SSM to guide the disaggregation algorithm. Therefore, some similarities can be expected with passive MW under relatively homogenous landscapes. But for heterogeneous landscapes, the SEE based algorithm

446 is expected to provide physically based additional details on the underlying SSM state. This issue
447 is further explored through the gain statistics discussed in the next section.

448 **5.3 Gain Statistics**

449 As mentioned earlier in section 4.2, the scale mismatch between in situ observations and
450 gridded remotely sensed SSM data can induce sampling error; therefore, gain statistics were
451 computed at coincident dates between coarse and finer resolution SSM data simultaneously
452 against in situ observations. Figures 6 display the map of gain statistics across CONUS of
453 various remotely sensed SSM products. The overall gains in SMAP-AP are observed in the
454 extremes of both directions. Less than half (37.8%) of the total SCAN sites observed positive
455 gains in bias, slope and correlations in SMAP-AP data (Figure 7). On the other hand, more than
456 50% of SCAN sites observed positive gains in both SMAP-E and TIR-Downscaled SSM
457 estimates for all the cases. Although at the majority of sites the SSM quality was improved with
458 SMAP-E data, the number of sites with positive gains is even higher with TIR-Downscaled (9-
459 km) compared to SMAP-E in all cases, but most particularly in the precision statistic. In
460 particular, the area where the SMAP-E and TIR products were questionable (Appalachia) shows
461 more positive gains in the TIR-downscaled SSM than in the SMAP-E.

462 At 3-km resolution, the relative overall gains in disaggregating passive MW SSM
463 estimates from SMAP-A and TIR-Downscaled (3-km) compared to SCAN observations are
464 shown in Figure 6 (right). The figure is notable for the preponderance of sites showing a negative
465 overall gain, mostly concentrated in the western U.S. as well as the Mississippi River valley. On
466 the other hand, the TIR-Downscaled SSM exhibited many positive gains, although most of the
467 overall gains were small –*i.e.*, within ± 0.1 (>91%). In all cases (efficiency; precision; and

accuracy), the percent of sites with positive gains in TIR-Down (3-km) is higher than the SMAP-A by a factor of nearly 3 (Figure 8).

Figure 7 also shows the percent of sites with positive gains with SSM data at 9-km resolution compared to coarse resolution passive MW and SCAN point observations. The results from gain statistics suggest that there is a clear improvement in representation of SSM at the intermediate scale with SMAP-E data compared to the SMAP-AP product. More than half of the locations with positive gains indicate that the intermediate scale SM from SMAP-E is of superior quality to the coarse resolution passive MW against in situ observations. The TIR-based SM at both scales (3 and 9-km resolution) appears to slightly better represent the SM conditions at higher resolution compared to other products with the maximum number of sites having positive gains. Again, however, Figure 6 indicates that the magnitude of the gains is modest (≈10%) and the difference between the SMAP-E and TIR-Downscaled products is very small in most cases.

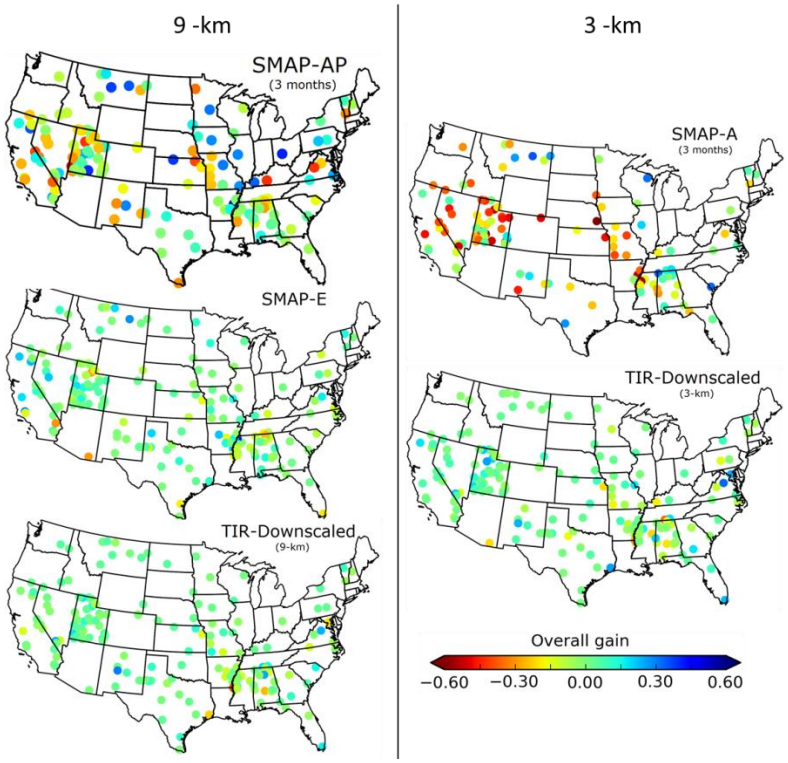

Figure 6: Overall gain statistics between NRCS SCAN observations relative to SMAP-E/SMAP-AP and TIR-Down SSM at 9-km scale (right) and SMAP-A and TIR-Down at 3-km (Right). [SMAP-A and SMAP-AP gains are based on 3 months data while SMAP-E as well as TIR-Downscaled (3 & 9-km) are based on 19 months]

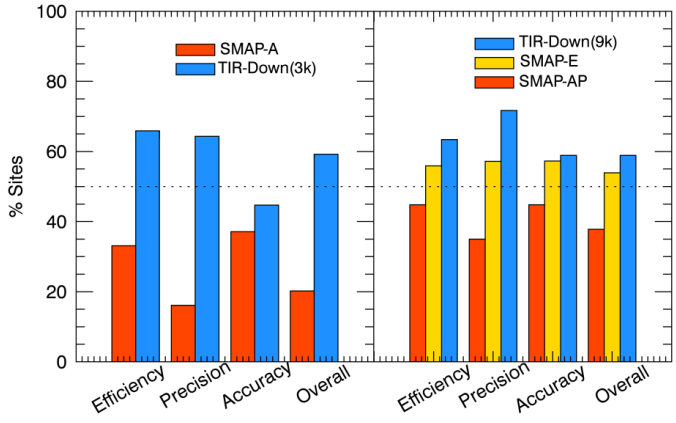

Figure 7: Percent of SCAN sites with positive gain in moving from coarse to finer resolution against SCAN in-situ observations.

5.4 Effect of Vegetation Cover

492 It has been argued that the MW SSM signals are attenuated by thick vegetation cover,
493 especially with higher frequency bands like C- and X- (Albergel et al., 2011; Brocca et al.,
494 2011). With L-band radars, like that of SMAP, the sensitivity to vegetation cover is
495 comparatively reduced, yet errors are still higher over vegetated land surfaces compared to bare
496 soils (Konings et al., 2017). With the ALEXI model, sensitivities decrease as surface moisture
497 content reaches either the wilting point or field capacity (Hain et al., 2011). The partitioning of
498 system (canopy + surface) energy fluxes to surface evaporation in the ALEXI model is limited
499 by the fraction of vegetation cover. The vegetation effects of both the SMAP and ALEXI
500 products could, in part, explain the spatial disparities identified in the east (and far west) and the
501 more central/western states (Figures 4 and 5). In this section, we analyze the effect of vegetation
502 cover on coarse and disaggregated SSM using an independent third SSM source, NLDAS2 (Xia
503 et al., 2012) (Mosaic of Noah and Variable Infiltration Capacity (VIC) LSMs). The analysis does
504 not assume that the LSMs are accurate; models may have their own biases and errors associated
505 with them. The assumption is that the physically-derived SSM from LSM models will not have
506 any vegetative effects associated. The analyses performed using LSM are only to assess the
507 relative dynamics of both remotely sensed SSM products under various vegetative scenarios
508 against a common independent data source. Due to limited data availability resulting in small
509 sample sizes, as well as their relatively poor performance in the previous analyses, the SMAP-A
510 and -AP products are omitted from this analysis. Also, since SCAN sites are located in
511 agricultural regions, the vegetation cover typically does not go beyond 65-70% and hence cannot
512 be used to assess the complete extent of vegetative impacts.

513 Figure 8 shows the annual mean fraction of vegetation cover derived using MODIS LAI
514 (Myneni et al., 2002) over CONUS for the year 2016. In most of the central and western part of

CONUS, mean vegetation cover is less than 40%, thus the surface conditions are readily accessible through both MW and TIR based sensing platforms. The frequency distribution of the statistical comparison between SMAP-E and TIR-Downscaled (9-km) SSM as a function of mean fractional vegetation cover is shown in Figure 9. The figure clearly indicates the effect of vegetation cover on the statistical relationship between the two soil moisture products. With vegetation cover less than 40%, both SM products seems to be strongly related with $r > 0.75$ (bias nearly 0.0 m^3m^{-3} and ubRMSD < 0.03 m^3m^{-3}). However, a sharp decline in correlation with a simultaneous steep rise in bias and ubRMSD was observed with vegetation cover beyond 70%. For vegetation cover between 40 and 70%, the correlation drops but the fall is relatively less steep compared to vegetation cover of greater than 70%.

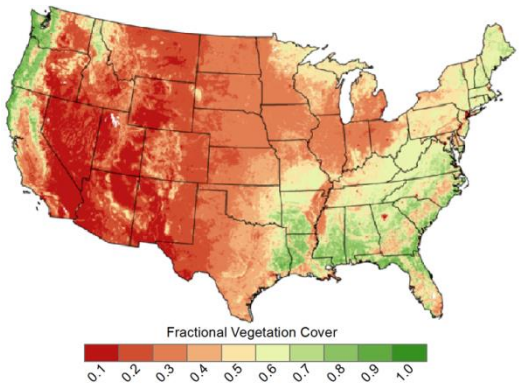

Figure 8: Fraction of Vegetation Cover over CONUS

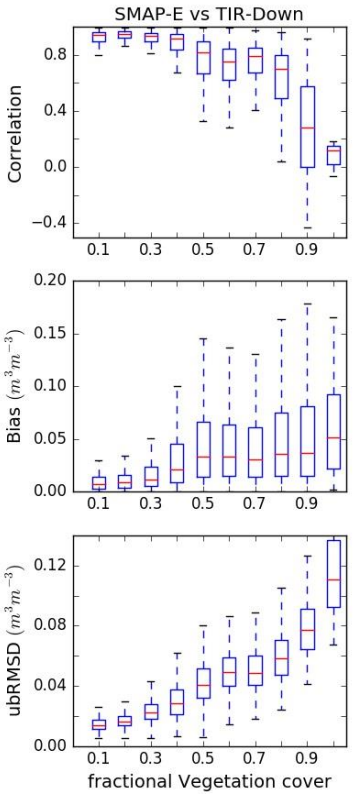

Figure 9. Comparison of SMAP-E and TIR-Downscaled SSM Products as a function of fractional vegetation cover (9-km)

Figure 9 shows the effects of vegetation cover on remotely sensed SSM products; however, the analysis does not illustrate the effects of vegetation on individual datasets. Therefore, the NLDAS2 SSM product was used as an independent source to assess the vegetative effect on the individual remotely sensed SSM products. Figure 10 shows the statistical comparison between the two remotely sensed SSM products against NLDAS2 SM data as a function of vegetation cover. Not surprisingly, both SMAP-E and TIR-Down SSM data showed similar responses to the NLDAS2 SSM product as a function of vegetation cover. The correlation tends to be higher ($r > 0.5$) under 10-40% vegetation cover with a general decreasing trend thereafter. Similarly, biases tend to be lower (< 0.05 m^3m^{-3}) for vegetation cover less than 40% and increase with higher vegetation cover. The overall ubRMSD for SMAP-E is 0.044 (m^3m^{-3}) and for TIR-down is 0.047

543 (m^3m^{-3}) compared to NLDAS2, also showing a relatively lower values with sparse vegetation
544 and higher ubRMSD with higher vegetation cover. Overall, the two products performed similarly
545 indicating that both remotely sensed SSM estimates relationship with NLDAS2 is strong under
546 low vegetation and it diminished as vegetation cover increases, particularly around 70%.

547 As mentioned earlier, since both products begin with the same basic source (the native
548 SMAP MW data) some similarity in behavior is to be expected; rather it is the downscaling
549 methods (IFOV interpolation vs TIR-based) that are being compared. These results indicate that
550 the two methods produce very similar results when compared to both in situ data and an
551 independent gridded source. Further, there is a discrepancy in the SSM layer depth definition of
552 the NLDAS2 product. NLDAS2 had surface SM defined as mean moisture content between 0-10
553 cm depth whereas MW and TIR-Downscaled SSM are estimates of typically < 5 cm depth.

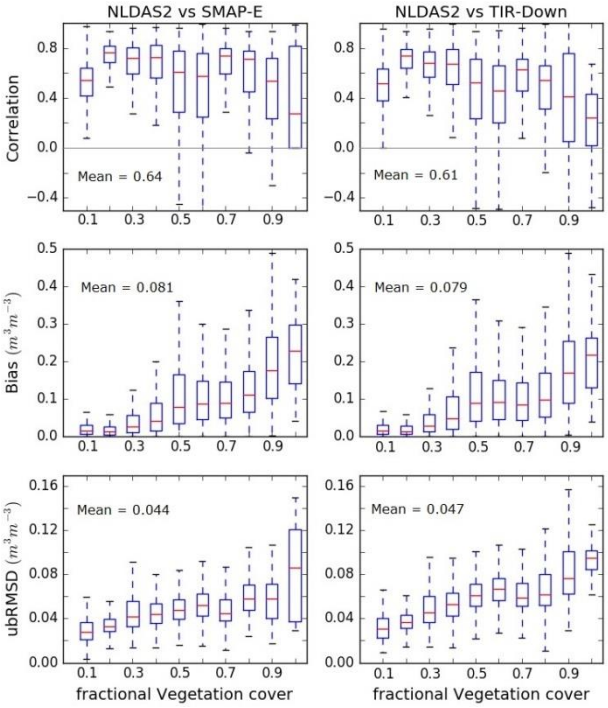

554

555

Figure 10. Results of statistical comparison between NLDAS2 vs SMAP-E (right-panel) and NLDAS vs TIR-Downscaled (left-panel) SSM over CONUS as a function of fractional vegetation cover.

Overall, the results of the present study are similar to those recently reported in the literature at varying spatial scales and locations: Chen et al., (2017) -- *r*: -0.3-0.72, RMSD: 0.06-0.27; Malbéteau et al., (2016) -- *r*: 0.70-0.94, RMSD: 0.07-0.09; Merlin et al., (2015) -- *r*: -0.22-0.64, RMSD:0.05-0.32; Molero et al., (2016) -- *r*: 0.35-0.47, ubRMSD:0.04-0.12; Colliander et al., (2017) -- *r:* 0.6(1-km) and 0.7(3-km); ubRMSD: 0.05(1-km) and 0.04(3-km). Most of these earlier studies are short term and site specific with multiple in situ observations possibly within a single pixel resolution and thus offer better representation of the SSM conditions. However, in this study single in situ observations per pixel were available but the approach was applied at the continental scale encompassing multiple climate and ecological regimes for a relatively longer time period. Despite these differences, the correlation and error results obtained are comparable to earlier studies.

6 Potential Error Sources

The accuracy of SEE based disaggregation model is dependent upon the accuracy of: (a) SEE estimation and (b) the relationship between SSM and SEE. SEE accuracy can be associated with ALEXI estimation of surface evaporation. As mentioned earlier, ALEXI estimates the total ET and then partitions between soil evaporation and canopy transpiration, which leads to errors in surface evaporation especially in areas of high vegetation cover (Figure 9 and 10). A brief ALEXI model description is presented in appendix A2. Further, the assumption behind using Hamon-PET as a proxy of surface potential evaporation, could further add to the error in SEE

579 estimation. Next, error in the use of the linear vs non-linear model to relate SEE with SSM is still
580 unclear. Earlier studies [such as Merlin et al., (2010,2013, 2012)] used the non-linear approach,
581 while later analyses [such as Merlin et al., (2015)] showed that the linear model performed better
582 than non-linear in dry and arid conditions of Australia. However, recent studies by Djamai et al.,
583 (2015) and Mishra et al., (2017) suggested that the non-linear models are better suited for wet
584 and humid climatic conditions than the linear model. Our analysis at continental scale showed no
585 significant difference between the overall statistics from the two models. This study employed
586 the non-linear model throughout CONUS including the dry domain in the western U.S.
587

588 **Conclusions**

589 This study investigated the effectiveness of the SMAP downscaled products against the soil
590 evaporative based disaggregation scheme over CONUS compared to *in situ* data from 180+
591 USDA observation sites. The study evaluated the performance of the downscaled SSM and the
592 SMAP SSM estimates at both 9- and 3-km spatial scales consistent with SMAP SSM products.
593 Since both the 9- and 3-km downscaling were based on resampling of the ALEXI TIR data from
594 its native 4.7-km resolution, perhaps not surprisingly, the statistics of the 3-km downscaled TIR
595 data were similar as in the 9-km case. Clearly, the resampling did not materially affect the
596 results. It should be noted that the results of SMAP-A and SMAP-AP comparisons are based on
597 a sample size of only 3 months (84-88 days) while SMAP-E are based on 19 months (607 days)
598 of data.

599 The 3-km SMAP active radar product statistics were inferior to the other SSM products with
600 the exception of bias (= 0.008 m^3m^{-3}). There was a considerable deterioration in the SMAP-A (3-

km) product retrieved from the active radar compared to SCAN observations (r = 0.16 and ubRMSD = 0.14 m^3m^{-3}). The radar performed most poorly in the western U.S. The questionable results of the active radar addition, although based on a very small sample and with limited results from other studies available, nevertheless appear to bring the approach of merging active and passive estimation to downscale SSM into question. The success of such an approach is contingent upon the accuracy of active radar SSM estimates.

The 9-km SMAP-E and TIR-Downscaled products offered only modest improvements to the coarse scale SMAP-P (36-km) SSM in terms of overall statistical comparison to the SCAN data. However, when viewed spatially, there were some improvements (≈10%) in some locations across CONUS, particularly in arid climates and in the Appalachian region. The TIR-Downscaled SSM data correlated strongly with the SMAP-E SSM product both spatially and temporally. Since the SMAP-E is merely a statistical interpolation of the original SMAP-P data streams, the failure of the physically-based TIR downscaling scheme to improve upon it substantially is somewhat puzzling at this time. The failure of both the SMAP interpolation and SEE downscaling methods to significantly improve the overall coarse scale SMAP-P SSM estimates seems to indicate that the downscaling approach may not be substantially effective in improving the SSM quality at large spatio-temporal scales. Interestingly, previous studies by Malbéteau et al.,(2016); Mishra et al., (2017); Molero et al., (2016) etc. have demonstrated the capability of the SEE method to significantly improve other MW SSM data such as AMSR-E and SMOS typically applied at smaller spatio-temporal scales.

Although of limited value in the present study, the TIR-based disaggregation approach has potential for long-term agricultural and hydrological analysis of SSM data sets, particularly

623 from the X and C-band sensors. For hydro-meteorological and agricultural applications an
624 intermediate spatial scale of 9-km or less is preferred to the coarse radiometer scale, and the
625 disaggregation scheme has been found to be efficient in other studies. The gain statistics show
626 that the highest number of SCAN site (~60%) locations with TIR-Down (9-km) data had
627 positive overall gains compared to only 54% with SAMP-E. The results indicate that, although
628 the overall statistics at CONUS scale are similar for the two SSM products, yet at the point scale
629 there is a difference between the statistics with TIR-Downscaled data outperforming SMAP-E at
630 nearly 6% more sites. Further, the scheme is found to be most efficient under low to moderately
631 thick vegetation cover and therefore may supplement agricultural applications effectively.
632 Although the TIR-Down SM was compared and validated at the 9-km scale, the effective
633 resolution of the product was 4.7-km.

634

635

636

637

638

639

640

641

642

643

644

645

Appendix

A1. Summary statistics of remotely sensed SSM products against in-situ observations at SCAN sites with coincident dates.

Table A1: Summary statistics at SCAN sites with coincident data points

	No. of SCAN sites	Average No. Days	Correlation (r)	Slope	Bias	ubRMSD
Active			0.17	0.22	-0.03	0.089
Passive	113	21	0.46	0.45	-0.014	0.052
TIR-Down(3k)			0.46	0.48	-0.013	0.052
Active/Passive			0.40	0.29	-0.005	0.063
Passive	136	27	0.46	0.51	-0.014	0.051
TIR-Down(9k)			0.45	0.51	-0.016	0.052
Enhanced			0.54	0.44	-0.014	0.061
Passive	176	267	0.55	0.45	-0.014	0.059
TIR-Down(9k)			0.54	0.46	-0.016	0.061

A2. ALEXI Model Description

The Atmosphere-Land Exchange Inverse (ALEXI; Fig. A1) model was formulated as an extension to the two-source energy balance (TSEB) model of Norman et al. (1995), which addressed many of issues limiting surface energy flux monitoring from TIR remote sensing platforms. The two-source approximation treats the radiometric temperature (T_{RAD}) of a vegetated surface as the ensemble average of the nominal temperature of the soil (T_s) and vegetation (T_c) components, partitioned by the fractional vegetation cover ($f(\theta)$) apparent from the sensor view angle (θ):

$$T_{RAD} \approx \{f(\theta)T_c + [1 - f[\theta]]T_s\}, \quad (1)$$

where $f(\theta)$ is represented by:

$$f(\theta) = 1 - \exp\left(\frac{-0.5\ LAI}{\cos\theta}\right). \quad (2)$$

The TSEB separately balances the energy budgets for the soil and vegetation components of

665 the system, solving for total system fluxes of net radiation (*RN*), latent heat (*LE*, or ET in units of
666 water flux), sensible heat (*H*) and ground heat conduction (*G*), such that $RN = H + LE + G$.

667 For regional-scale applications, the TSEB has been coupled with an atmospheric boundary
668 layer (ABL) model (McNaughton and Spriggs, 1986) to internally simulate land-atmosphere
669 feedback (Anderson et al. 1997). In ALEXI, the TSEB is applied at two times during the
670 morning ABL growth phase using TIR data obtained from a geostationary platform (e.g., GOES,
671 Meteosat, MT-SAT) at 5-10 km resolution. The ABL component of ALEXI relates the rise in T_a
672 in the mixed layer over the observation time interval to the time-integrated influx of *H* from the
673 surface, thus providing energy closure for the TSEB land-surface component.

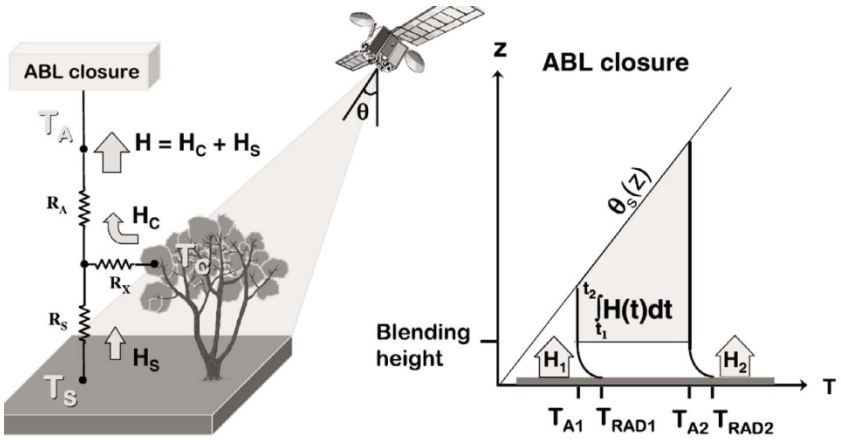

674

675 Figure A1: Schematic of the ALEXI model (taken from Anderson et al., 2007)
676

677 For operational applications, the coupling of the ABL within ALEXI is advantageous
678 because it moves the upper boundary condition in temperature from the near-surface to the
679 "blending height", where conditions are more uniform at a spatial scale of a geostationary
680 satellite thermal pixel and can be more accurately specified. Furthermore, as a result of this
681 configuration ALEXI uses only time-differential temperature signals, thereby minimizing flux

errors due to absolute sensor calibration and atmospheric correction (Kustas et al., 2001). The primary radiometric signal is the morning surface temperature rise, while the ABL model component uses only the general slope (lapse rate) of the atmospheric temperature profile (Anderson et al., 1997), which is more reliably analyzed from synoptic radiosonde data than is the absolute temperature reference. Further description of ALEXI and ancillary datasets needed for continental-scale applications are provided by Anderson et al., (1997) and Mecikalski et al., (1999).

Conflict of Interest

The authors declare no conflict of interest.

Acknowledgements

This study was supported by NASA Headquarters under the NASA Earth and Space Science Fellowship (NESSF) Program-Grant NNX15AN58H (PI - John R. Mecikalski) and NASA Cooperative Agreement NNM11AA01A. The authors are also thankful to agencies such as NASA and NRCS for making soil moisture data publically available.

References

Aghakouchak, A., Farahmand, A., Melton, F.S., Teixeira, J., Anderson, M.C., Wardlow, B.D., Hain, C.R., 2015. Remote sensing of drought : Progress , challenges and opportunities. Rev. Geophys. 53, 452–480. doi:10.1002/2014RG000456.Received

Albergel, C., Zakharova, E., Calvet, J.-C., Zribi, M., Pardé, M., Wigneron, J.-P., Novello, N., Kerr, Y., Mialon, A., Fritz, N.-D., 2011. A first assessment of the SMOS data in southwestern France using in situ and airborne soil moisture estimates: The CAROLS airborne campaign. Remote Sens. Environ. 115, 2718–2728. doi:10.1016/j.rse.2011.06.012

Anderson, M.C., Kustas, W.P., Norman, J.M., Hain, C.R., Mecikalski, J.R., Schultz, L., Gonzlez-Dugo, M.P., Cammalleri, C., D'Urso, G., Pimstein, A., Gao, F., 2011. Mapping daily evapotranspiration at field to continental scales using geostationary and polar orbiting satellite imagery. Hydrol. Earth Syst. Sci. 15, 223–239. doi:10.5194/hess-15-223-2011

Anderson, M.C., Norman, J.M., Diak, G.R., Kustas, W.P., 1997. A Two-Source Time-Integrated Model for Estimating Surface Fluxes Using Thermal Infrared Remote Sensing. Remote Sens. Environ. 60, 195–216. doi:10.1016/S0034-4257(96)00215-5

713 Anderson, M.C., Norman, J.M., Mecikalski, J.R., Otkin, J.A., Kustas, W.P., 2007. A
714 climatological study of evapotranspiration and moisture stress across the continental United
715 States based on thermal remote sensing: 2. Surface moisture climatology. J. Geophys. Res.
716 D Atmos. 112. doi:10.1029/2006JD007507

717 Bindlish, R., Jackson, T., Sun, R., Cosh, M., Yueh, S., Dinardo, S., 2009. Combined passive and
718 active microwave observations of soil moisture during CLASIC. IEEE Geosci. Remote
719 Sens. Lett. 6, 644–648. doi:10.1109/LGRS.2009.2028441

720 Brocca, L., Hasenauer, S., Lacava, T., Melone, F., Moramarco, T., Wagner, W., Dorigo, W.,
721 Matgen, P., Martínez-Fernández, J., Llorens, P., Latron, J., Martin, C., Bittelli, M., 2011.
722 Soil moisture estimation through ASCAT and AMSR-E sensors: An intercomparison and
723 validation study across Europe. Remote Sens. Environ. 115, 3390–3408.
724 doi:10.1016/j.rse.2011.08.003

725 Brocca, L., Melone, F., Moramarco, T., Morbidelli, R., 2010. Spatial-temporal variability of soil
726 moisture and its estimation across scales. Water Resour. Res. 46, 1–14.
727 doi:10.1029/2009WR008016

728 Brown, M.E., Escobar, V., Moran, S., Entekhabi, D., O'Neill, P.E., Njoku, E.G., Doorn, B.,
729 Entin, J.K., Brown, M.E., Escobar, V., Moran, S., Entekhabi, D., O'Neill, P.E., Njoku, E.G.,
730 Doorn, B., Entin, J.K., 2013. NASA's Soil Moisture Active Passive (SMAP) Mission and
731 Opportunities for Applications Users. Bull. Am. Meteorol. Soc. 94, 1125–1128.

732 Carlson, T., 2007. An Overview of the "Triangle Method" for Estimating Surface
733 Evapotranspiration and Soil Moisture from Satellite Imagery. Sensors 7, 1612–1629.
734 doi:10.3390/s7081612

735 Carlson, T.N., Dodd, J.K., Benjamin, S.G., Cooper, J.N., 1981. Satellite Estimation of the
736 Surface Energy Balance, Moisture Availability and Thermal Inertia. J. Appl. Meteorol. 20,
737 67–87. doi:10.1175/1520-0450(1981)020<0067:SEOTSE>2.0.CO;2

738 Chan, S., Bindlish, R., Neill, P.O., Jackson, T., Texas, T.C.U., U, J.W.M., U, X.W.M., Valencia,
739 E.L.U., Denmark, F.U.T.U., Su, Z., Twente, R.V.D.V.U., Tsukuba, J.A.U., Noaa, M.P.,
740 Cesbio-cnes, Y.K., 2017. Development and Validation of The SMAP Enhanced Passive
741 Soil Moisture Product 2539–2542.

742 Chauhan, N.S., Miller, S., Ardanuy, P., 2003. Spaceborne soil moisture estimation at high
743 resolution: A microwave-optical/IR synergistic approach. Int. J. Remote Sens. 24, 4599–
744 4622.

745 Chen, N., He, Y., Zhang, X., 2017. NIR-Red Spectra-Based Disaggregation of SMAP Soil
746 Moisture to 250 m Resolution Based on SMAPEx-4/5 in Southeastern Australia. Remote
747 Sens. 9, 51. doi:10.3390/rs9010051

748 Colliander, A., 2017. SMAP/In Situ Core Validation Site Land Surface Parameters Match-Up
749 Data, Version 1 SPL2SMAP_S. doi:http://dx.doi.org/10.5067/DXAVIXLY18KM

750 Colliander, A., Fisher, J.B., Halverson, G., Merlin, O., Misra, S., Bindlish, R., Jackson, T.J.,
751 Yueh, S., 2017. Spatial Downscaling of SMAP Soil Moisture Using MODIS Land Surface
752 Temperature and NDVI During SMAPVEX15. IEEE Geosci. Remote Sens. Lett. 14, 2107–

2111. doi:10.1109/LGRS.2017.2753203

Cosgrove, B.A., 2003. Real-time and retrospective forcing in the North American Land Data Assimilation System (NLDAS) project. J. Geophys. Res. 108, 8842. doi:10.1029/2002JD003118

Crow, W.T., Berg, A.A., Cosh, M.H., Loew, A., Mohanty, B.P., Panciera, R., De Rosnay, P., Ryu, D., Walker, J.P., 2012. Upscaling sparse ground-based soil moisture observations for the validation of coarse-resolution satellite soil moisture products. Rev. Geophys. 50. doi:10.1029/2011RG000372

Das, N.N., Dunbar, S.R., 2017. Level 2 SMAP/Sentinel Active/Passive Soil Moisture Product Specification Document. Pasadena, California.

Das, N.N., Entekhabi, D., Kim, S., Yueh, S., O'Neill, P., 2016. Combining SMAP and Sentinel data for high-resolution Soil Moisture product, in: 2016 IEEE International Geoscience and Remote Sensing Symposium (IGARSS). IEEE, pp. 129–131. doi:10.1109/IGARSS.2016.7729024

Das, N.N., Entekhabi, D., Njoku, E.G., 2011. An algorithm for merging SMAP radiometer and radar data for high-resolution soil-moisture retrieval. IEEE Trans. Geosci. Remote Sens. 49, 1504–1512. doi:10.1109/TGRS.2010.2089526

Djamai, N., Magagi, R., Goita, K., Merlin, O., Kerr, Y., Walker, A., 2015. Disaggregation of SMOS soil moisture over the Canadian Prairies. Remote Sens. Environ. 170, 255–268. doi:10.1016/j.rse.2015.09.013

Entekhabi, D., Njoku, E.G., O'Neill, P.E., Kellogg, K.H., Crow, W.T., Edelstein, W.N., Entin, J.K., Goodman, S.D., Jackson, T.J., Johnson, J., Kimball, J., Piepmeier, J.R., Koster, R.D., Martin, N., McDonald, K.C., Moghaddam, M., Moran, S., Reichle, R., Shi, J.C., Spencer, M.W., Thurman, S.W., Tsang, L., Van Zyl, J., 2010a. The soil moisture active passive (SMAP) mission. Proc. IEEE 98, 704–716. doi:10.1109/JPROC.2010.2043918

Entekhabi, D., Reichle, R.H., Koster, R.D., Crow, W.T., 2010b. Performance Metrics for Soil Moisture Retrievals and Application Requirements. J. Hydrometeorol. 11, 832–840. doi:10.1175/2010JHM1223.1

Fang, B., Lakshmi, V., 2014. AMSR-E Soil Moisture Disaggregation Using MODIS and NLDAS Data, in: Lakshmi, V., Alsdorf, D., Anderson, M., Biancamaria, S., Cosh, M., Entin, J., Huffman, G., Kustas, W., Oevelen, P., Painter, T., Parajka, J., Rodell, M., Rudiger, C. (Eds.), Remote Sensing of the Terrestrial Water Cycle. John Wiley & Sons, Inc, Hoboken, NJ, pp. 277–304.

Hain, C.R., Crow, W.T., Anderson, M.C., Mecikalski, J.R., 2012. An ensemble Kalman filter dual assimilation of thermal infrared and microwave satellite observations of soil moisture into the Noah land surface model. Water Resour. Res. 48. doi:10.1029/2011WR011268

Hain, C.R., Crow, W.T., Mecikalski, J.R., Anderson, M.C., Holmes, T., 2011. An intercomparison of available soil moisture estimates from thermal infrared and passive microwave remote sensing and land surface modeling. J. Geophys. Res. Atmos. 116, 1–18. doi:10.1029/2011JD015633

793 Hamon, W.R., 1963. Computation of Direct Runoff Amounts From Storm Rainfall. Int. Assoc.
794 Sci. Hydrol. Pub. 63, 52–62.

795 Kerr, Y.H., Waldteufel, P., Wigneron, J.-P., Delwart, S., Cabot, F., Boutin, J., Escorihuela, M.-J.,
796 Font, J., Reul, N., Gruhier, C., Juglea, S.E., Drinkwater, M.R., Hahne, A., Martín-Neira, M.,
797 Mecklenburg, S., 2010. The SMOS Mission: New Tool for Monitoring Key Elements ofthe
798 Global Water Cycle. Proc. IEEE 98, 666–687. doi:10.1109/JPROC.2010.2043032

799 Kim, J., Hogue, T.S., 2012. Improving spatial soil moisture representation through integration of
800 AMSR-E and MODIS products. IEEE Trans. Geosci. Remote Sens. 50, 446–460.

801 Knipper, K.R., Hogue, T.S., Franz, K.J., Scott, R.L., 2017. Downscaling SMAP and SMOS soil
802 moisture with moderate-resolution imaging spectroradiometer visible and infrared products
803 over southern Arizona. J. Appl. Remote Sens. 11. doi:10.1117/1.JRS.11.026021

804 Komatsu, T.S., 2003. Towards a robust phenomenological expression of evaporation efficiency
805 for unsaturated soil surfaces. J. Appl. Meteorol. 42, 1330–1334.

806 Konings, A.G., Piles, M., Das, N.N., Entekhabi, D., 2017. L-band vegetation optical depth and
807 effective scattering albedo estimation from SMAP. Remote Sens. Environ. 198, 460–470.
808 doi:10.1016/J.RSE.2017.06.037

809 Kustas, W.P., Diak, G.R., Norman, J.M., 2001. Time Difference Methods for Monitoring
810 Regional Scale Heat Fluxes with Remote Sensing, in: Lakshmi, V., Albertson, J., Schaake,
811 J. (Eds.), Land Surface Hydrology, Meteorology, and Climate: Observations and Modeling,
812 Water Science and Application. American Geophysical Union, Washington, D. C.
813 doi:10.1029/WS003

814 Lee, T.J., Pielke, R.A., 1992. Estimating the soil surface specific humidity. J. Appl. Meteorol.
815 31, 480–484.

816 Leng, P., Li, Z.-L., Duan, S.-B., Gao, M.-F., Huo, H.-Y., 2017a. A practical approach for
817 deriving all-weather soil moisture content using combined satellite and meteorological data.
818 ISPRS J. Photogramm. Remote Sens. 131, 40–51. doi:10.1016/j.isprsjprs.2017.07.013

819 Leng, P., Li, Z.-L., Duan, S.-B., Tang, R., Gao, M.-F., 2017b. A Method for Deriving All-Sky
820 Evapotranspiration From the Synergistic Use of Remotely Sensed Images and
821 Meteorological Data. J. Geophys. Res. Atmos. 1–15. doi:10.1002/2017JD027880

822 Lievens, H., Reichle, R.H., Liu, Q., De Lannoy, G.J.M., Dunbar, R.S., Kim, S.B., Das, N.N.,
823 Cosh, M., Walker, J.P., Wagner, W., 2017. Joint Sentinel-1 and SMAP data assimilation to
824 improve soil moisture estimates. Geophys. Res. Lett. 44, 6145–6153.
825 doi:10.1002/2017GL073904

826 Malbéteau, Y., Merlin, O., Molero, B., Rüdiger, C., Bacon, S., 2016. DisPATCh as a tool to
827 evaluate coarse-scale remotely sensed soil moisture using localized in situ measurements:
828 Application to SMOS and AMSR-E data in Southeastern Australia. Int. J. Appl. Earth Obs.
829 Geoinf. 45, 221–234. doi:10.1016/j.jag.2015.10.002

830 McCabe, M.F., Gao, H., Wood, E.F., 2005. Evaluation of AMSR-E-Derived Soil Moisture
831 Retrievals Using Ground-Based and PSR Airborne Data during SMEX02. J.

Hydrometeorol. 6, 864–877. doi:10.1175/JHM463.1

McNaughton, K.G., Spriggs, T.W., 1986. A mixed-layer model for regional evapotranspiration. Boundary-Layer Meteorol. 34, 243–262.

Mecikalski, J.R., Diak, G.R., Anderson, M.C., Norman, J.M., 1999. Estimating Fluxes on Continental Scales Using Remotely Sensed Data in an Atmospheric–Land Exchange Model. J. Appl. Meteorol. doi:10.1175/1520-0450(1999)038<1352:EFOCSU>2.0.CO;2

Merlin, O., Al Bitar, A., Walker, J.P., Kerr, Y., 2010. An improved algorithm for disaggregating microwave-derived soil moisture based on red, near-infrared and thermal-infrared data. Remote Sens. Environ. 114, 2305–2316. doi:10.1016/j.rse.2010.05.007

Merlin, O., Duchemin, B., Hagolle, O., Jacob, F., Coudert, B., Chehbouni, G., Dedieu, G., Garatuza, J., Kerr, Y., 2010. Disaggregation of MODIS surface temperature over an agricultural area using a time series of Formosat-2 images. Remote Sens. Environ. 114, 2500–2512. doi:10.1016/j.rse.2010.05.025

Merlin, O., Escorihuela, M.J., Mayoral, M.A., Hagolle, O., Al Bitar, A., Kerr, Y., 2013. Self-calibrated evaporation-based disaggregation of SMOS soil moisture: An evaluation study at 3km and 100m resolution in Catalunya, Spain. Remote Sens. Environ. 130, 25–38. doi:10.1016/j.rse.2012.11.008

Merlin, O., Malbeteau, Y., Notfi, Y., Bacon, S., Er-Raki, S., Khabba, S., Jarlan, L., 2015. Performance metrics for soil moisture downscaling methods: Application to DISPATCH data in central Morocco. Remote Sens. 7, 3783–3807. doi:10.3390/rs70403783

Merlin, O., Rudiger, C., Al Bitar, A., Richaume, P., Walker, J.P., Kerr, Y.H., 2012. Disaggregation of SMOS Soil Moisture in Southeastern Australia. IEEE Trans. Geosci. Remote Sens. 50, 1556–1571. doi:10.1109/TGRS.2011.2175000

Merlin, O., Walker, J., Chehbouni, A., Kerr, Y., 2008. Towards deterministic downscaling of SMOS soil moisture using MODIS derived soil evaporative efficiency. Remote Sens. Environ. 112, 3935–3946. doi:10.1016/j.rse.2008.06.012

Miliaresis, G.C., Argialas, D.P., 1999. Segmentation of physiographic features from the global digital elevation model/GTOPO30. Comput. Geosci. 25, 715–728. doi:10.1016/S0098-3004(99)00025-4

Mishra, V., Cruise, J., Mecikalski, J., Hain, C., Anderson, M., 2013. A Remote-Sensing Driven Tool for Estimating Crop Stress and Yields. Remote Sens. 5, 3331–3356. doi:10.3390/rs5073331

Mishra, V., Cruise, J.F., Hain, C.R., Mecikalski, J.R., Anderson, M.C., 2017. Development of Soil Moisture Profiles Through Coupled Microwave-Thermal Infrared Observations in the Southeastern United States. Hydrol. Earth Syst. Sci. Discuss. 1–34. doi:10.5194/hess-2017-351

Molero, B., Merlin, O., Malbéteau, Y., Al Bitar, A., Cabot, F., Stefan, V., Kerr, Y., Bacon, S., Cosh, M.H., Bindlish, R., Jackson, T.J., 2016. SMOS disaggregated soil moisture product at 1km resolution: Processor overview and first validation results. Remote Sens. Environ. 180,

361–376. doi:10.1016/j.rse.2016.02.045

Myneni, R.B., Hoffman, S., Knyazikhin, Y., Privette, J.L., Glassy, J., Tian, Y., Wang, Y., Song, X., Zhang, Y., Smith, G.R., Lotsch, A., Friedl, M., Morisette, J.T., Votava, P., Nemani, R.R., Running, S.W., 2002. Global products of vegetation leaf area and fraction absorbed PAR from year one of MODIS data. Remote Sens. Environ. 83, 214–231. doi:10.1016/S0034-4257(02)00074-3

Narayan, U., Lakshmi, V., 2008. Characterizing subpixel variability of low resolution radiometer derived soil moisture using high resolution radar data. Water Resour. Res. 44, n/a–n/a. doi:10.1029/2006WR005817

Njoku, E.G., Jackson, T.J., Lakshmi, V., Chan, T.K., Nghiem, S. V., 2003. Soil moisture retrieval from AMSR-E. IEEE Trans. Geosci. Remote Sens. 41, 215–228. doi:10.1109/TGRS.2002.808243

Noilhan, J., Planton, S., 1989. A simple parameterization of land surface processes for meteorological models. Mon. Weather Rev. 117, 536–549.

Owe, M., De Jeu, R., Walker, J., 2001. A methodology for surface soil moisture and vegetation optical depth retrieval using the microwave polarization difference index. IEEE Trans. Geosci. Remote Sens. 39, 1643–1654. doi:10.1109/36.942542

Paloscia, S., Macelloni, G., Santi, E., Koike, T., 2001. A multifrequency algorithm for the retrieval of soil moisture on a large scale using microwave data from SMMR and SSM/I satellites. IEEE Trans. Geosci. Remote Sens. 39, 1655–1661. doi:10.1109/36.942543

Peng, J., Loew, A., Merlin, O., Verhoest, N.E.C., 2017. A review of spatial downscaling of satellite remotely-sensed soil moisture. Rev. Geophys. doi:10.1002/2016RG000543

Penna, D., Brocca, L., Borga, M., Dalla Fontana, G., 2013. Soil moisture temporal stability at different depths on two alpine hillslopes during wet and dry periods. J. Hydrol. 477, 55–71. doi:10.1016/j.jhydrol.2012.10.052

Piles, M., Camps, A., Vall-Ilossera, M., Corbella, I., Rudiger, C., Panciera, R., Kerr, Y.H., Walker, J., 2011. Downscaling SMOS-derived soil moisture using MODIS visible/infrared data. IEEE Trans. Geosci. Remote Sens. 49, 3156–3166.

Piles, M., Petropoulos, G.P., Sánchez, N., González-Zamora, Á., Ireland, G., 2016. Towards improved spatio-temporal resolution soil moisture retrievals from the synergy of SMOS and MSG SEVIRI spaceborne observations. Remote Sens. Environ. 180, 403–417. doi:10.1016/j.rse.2016.02.048

Romano, N., 2014. Soil moisture at local scale: Measurements and simulations. J. Hydrol. 516, 6–20. doi:10.1016/j.jhydrol.2014.01.026

Rudiger, C., Su, C.H., Ryu, D., Wagner, W., 2016. Disaggregation of Low-Resolution L-Band Radiometry Using C-Band Radar Data. IEEE Geosci. Remote Sens. Lett. 13, 1425–1429. doi:10.1109/LGRS.2016.2583433

Sahoo, A.K., Houser, P.R., Ferguson, C., Wood, E.F., Dirmeyer, P.A., Kafatos, M., 2008.

909 Evaluation of AMSR-E soil moisture results using the in-situ data over the Little River
910 Experimental Watershed, Georgia. Remote Sens. Environ. 112, 3142–3152.
911 doi:10.1016/j.rse.2008.03.007

912 Sanchez-Ruiz, S., Piles, M., Sa´nchez, N., Marti´nez-Ferna´ndez, J., Vall-llossera, M., Camps,
913 A., 2014. Combining SMOS with visible and near/shortwave/thermal infrared satellite data
914 for high resolution soil moisture estimates. J. Hydrol. 516, 273–283.
915 doi:10.1016/j.jhydrol.2013.12.047

916 Santi, E., Paloscia, S., Pettinato, S., Brocca, L., Ciabatta, L., Entekhabi, D., 2018. On the synergy
917 of SMAP, AMSR2 AND SENTINEL-1 for retrieving soil moisture. Int. J. Appl. Earth Obs.
918 Geoinf. 65, 114–123. doi:10.1016/j.jag.2017.10.010

919 Schaefer, G.L., Cosh, M.H., Jackson, T.J., 2007. The USDA Natural Resources Conservation
920 Service Soil Climate Analysis Network (SCAN). J. Atmos. Ocean. Technol. 24, 2073–2077.
921 doi:10.1175/2007JTECHA930.1

922 Seneviratne, S.I., Corti, T., Davin, E.L., Hirschi, M., Jaeger, E.B., Lehner, I., Orlowsky, B.,
923 Teuling, A.J., 2010. Investigating soil moisture-climate interactions in a changing climate:
924 A review. Earth-Science Rev. 99, 125–161. doi:10.1016/j.earscirev.2010.02.004

925 Starks, P.J., Heathman, G.C., Ahuja, L.R., Ma, L., 2003. Use of limited soil property data and
926 modeling to estimate root zone soil water content. J. Hydrol. 272, 131–147.
927 doi:10.1016/S0022-1694(02)00260-3

928 Xia, Y., Mitchell, K., Ek, M., Sheffield, J., Cosgrove, B., Wood, E., Luo, L., Alonge, C., Wei,
929 H., Meng, J., Livneh, B., Lettenmaier, D., Koren, V., Duan, Q., Mo, K., Fan, Y., Mocko, D.,
930 2012. Continental-scale water and energy flux analysis and validation for the North
931 American Land Data Assimilation System project phase 2 (NLDAS-2): 1. Intercomparison
932 and application of model products. J. Geophys. Res. Atmos. 117, n/a–n/a.
933 doi:10.1029/2011JD016048

934

935

936